Article

One-Pot Green Synthesis and Biological Evaluation of Dimedone-Coupled 2,3-Dihydrofuran Derivatives to Divulge Their Inhibition Potential against Staphylococcal Thioredoxin Reductase Enzyme

Manjari Shukla, Ghanshyam Mali, Supriya Sharma, Sushobhan Maji, Vinay Kumar Yadav, Amit Mishra, Rohan D. Erande,* and Sudipta Bhattacharyya*

Read Online

ACCESS | Metrics & More | Article Recommendations | Supporting Information

ABSTRACT: New therapeutic leads are in global demand against multiple drug-resistant *Staphylococcus aureus*, as presently there is no drug of choice left to treat this pathogen. In the present work, we have designed, synthesized, and in vitro validated dimedone-coupled 2,3-dihydrofuran (DDHF)-based inhibitor scaffolds against Staphylococcal thioredoxin reductase (SaTR), a pivotal drug target enzyme of Gram-positive pathogens. Accordingly, a green multicomponent method that is both efficient and one pot has been optimized to synthesize DDHF derivatives. The synthesized DDHF derivatives were found to inhibit a purified SaTR enzyme. The best inhibitor derivative, DDHF20, inhibits SaTR as a competitive inhibitor for the NADPH binding site at low micromolar concentrations. DDHF20-capped silver nanoparticles are synthesized and characterized, and their bactericidal property has been checked in vitro. Furthermore, detailed in silico-based structure-guided functional studies have been carried out to uncover the plausible mode of action of DDHF20 as a potential anti-Staphylococcal therapeutic lead.
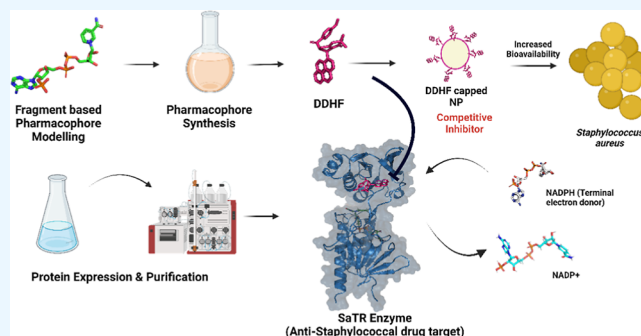
1. INTRODUCTION

The Gram-positive, nonmotile bacteria *Staphylococcus aureus* primarily colonizes human skin and the anterior nares. This organism is a part of normal skin microflora, asymptomatically carried over by 20−30% of the human population, and can be easily disseminated through aerosols and contaminated fomites.[1] Importantly, *S. aureus* is an opportunistic pathogen that can readily infect immunologically compromised patients and hospitalized individuals. Moreover, due to global emergence of multiple drug-resistant strains of *S. aureus*, it is becoming a threat to the healthcare industries owing to its capability to ensue myriad systemic infections.[2] Documented reports of hospital-associated methicillin-resistant *S. aureus* (HA-MRSA) and community-associated methicillin-resistant *S. aureus* (CA-MRSA) infections are catastrophically disrupting worldwide healthcare environments. The glycopeptide antibiotic vancomycin is the sole medication considered to be the best option for treating infections caused by methicillin-resistant *S. aureus* (MRSA). However, clinical usage of vancomycin is associated with severe nephrotoxicity, as well as emergence of vancomycin-resistant *S. aureus* (VRSA) strains leaves no drug of choice to treat this dreaded pathogen.[3] Therefore, new therapeutic leads are in urgent demand to tackle this superbug.

Earlier studies have indicated that Staphylococcal thioredoxin reductase (SaTR) enzyme is a novel drug target for small-

molecule-based antagonists.[4,5] During pathogenesis, virulent *S. aureus* strains use thiol-disulfide-based enzymatic redox cascade systems to neutralize the oxidative stress generated by the host immune cells. SaTR is the pivotal enzyme which acts as the terminal electron donor of several such enzyme cascade reactions which are responsible for Staphylococcal cellular defense against oxygen- and nitrogen-based reactive species generated by the host.[6] The functionality of the thiol-disulfide-based enzymatic redox cascade systems is highly reliant on the activity of SaTR. Hence, SaTR is indispensable for Staphylococcal growth and survival. Moreover, the eukaryotic thioredoxin reductase enzymes are significantly different from their bacterial counterparts as they carry selenocysteine instead of cysteine in the active site catalytic cleft, and their catalytic mechanism is significantly different from the bacterial counterparts.[7] Hence, SaTR enzyme has been suggested to be a valid drug target for deadly multiple drug-resistant species of *S. aureus*.[4,5]
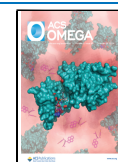
The present work is a result of our effort to search for small-molecule-based therapeutic lead/scaffolds which can cripple the thiol-disulfide-based enzymatic redox system of *S. aureus*. Herein, we applied an in silico fragment-based virtual screening approach to find plausible small-molecule-based inhibitor leads against SaTR enzyme. Intriguingly using an internal library of synthesized compounds, a dimedone-coupled dihydrofuran scaffold was found to be a promising candidate which may show SaTR inhibition by occupying the NADPH binding site.

Notably, 2,3-dihydrofuran is one of the significant class of heterocycles among furans, found in numerous biologically active natural products, therapeutic agents, and drug molecules.[8] Azadirachtin, austocystin A, clerodin, and bicunningines A and B are well-known examples of bioactive natural products identified based on the 2,3-dihydrofuran core structure.[9] In view of the medicinal importance, several drug candidates possessing the 2,3-dihydrofuran base skeleton has been proved to have a wide range of biological efficacy.[10,11] In addition, dimedone and its derivatives are also transpired to have an extensive set of biological activities, including anticarcinogenic, antioxidant, antihistaminic, and anticoagulant.[12−14] Moreover, the fascinating structure of dimedone (equilibrium with its tautomeric enol form[15]) and its chemical nature, low toxicity, ease of access, handling, moisture stability, and low cost makes it an appealing ingredient in a variety of chemical processes. In view of the intense medicinal profile of both 2,3-dihydrofuran and dimedone, they are emerged as key intermediates in many natural product synthesis and synthetic approaches till date.[16] Again, the combination product 2,3-dihydrofuro[3,2-c]dimedones revealed impressive pharmaceutical properties and are developed in prominence in last few decades.[17] In view of the promising medicinal profile and pharmaceutical demand, 2,3-dihydrofuro[3,2-c]dimedones need scalable methodologies and derivatives for further potential drug development.[18]

Herein, aiming to access the initially obtained 2,3-dihydrofuro[3,2-c]dimedone-based potential therapeutic lead against SaTR enzyme, we have developed a green one-pot approach to synthesize various substituted 2,3-dihydrofuro-[3,2-c]dimedone (DDHF) as well as their new derivatives. Herein, we report a simple, cost-effective one-pot strategy that delivered high quantities of 20 desirable 2,3-dihydrofuro[3,2-c]dimedone analogues with 9 novel products in an environment-friendly way with no intermediate isolation (Scheme 1).

Scheme 1. General Approaches to *trans*-2,3-Dihydrofurans
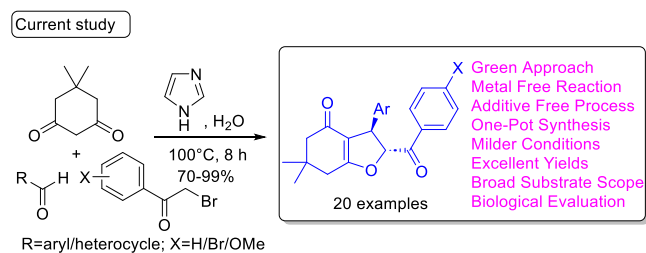
To our delight, the synthesized 2,3-dihydrofuran derivatives, at low to mid micromolar (μM) concentration ranges, have shown potential SaTR inhibition activities in vitro. Moreover, the synthesized 2,3-dihydrofuro[3,2-c]dimedone-capped silver nanoparticles (NPs) elicited anti-Staphylococcal activity in vitro. Detailed in silico-based studies also shed light on the
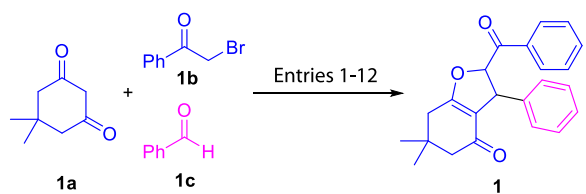
molecular mode of SaTR inhibition through competitively displacing SaTR-bound NADPH and thereby uncoupling the electron-transfer reaction from NADPH to flavin-adenine dinucleotide (FAD) and ultimately to SaTR's cognate substrate protein, oxidized thioredoxin (OxTrx).

2. RESULTS AND DISCUSSION

2.1. SaTR Mechanism of Action and Initial Fragment-Based Inhibitor Screening.
SaTR is a 35 kDa homodimeric flavoenzyme and is a member of the pyridine nucleotide disulfide oxidoreductase family. The enzyme participates in the Staphylococcal thiol-disulfide-based oxidoreductase enzyme cascade system, as the terminal electron donor and indispensable for the organism for survival. SaTR has the characteristic Rossmann fold and two distinct redox cofactor binding functional domains. One domain tightly binds the coenzyme FAD, while the other binds the recyclable redox cofactor NADPH. During the thiol-disulfide-based redox reaction, SaTR facilitates electron flow from incoming NADPH to bound FAD and finally to its cognate substrate, oxidized thioredoxin (OxTrx). Unlike the mammalian counterparts, during the catalytic cycle of SaTR, an interdomain catalytic twist of about $67°$ enables the crosstalk between the nicotinamide group of incoming NADPH and the isoalloxazine ring of the tightly bound FAD to flow electrons to the later prosthetic group. SaTR is one of the principal therapeutic targets for multiple drug-resistant *S. aureus*. So far, numerous research efforts have been conducted to design small-molecule-based inhibitors to selectively bind the substrate (OxTrx) binding site of SaTR. However, irrespective of decades of research, to date, no small-molecule-based inhibitors have been successfully designed and characterized to uncouple the catalytic flow of electrons from NADPH to FAD, which would subsequently impair the SaTR to donate electrons to its cognate substrate protein, OxTrx. The high-resolution crystal structure of SaTR enzyme has been solved previously (PDB ID: 4GCM). Herein, we used the high-resolution crystal structure of SaTR to perform structure-guided fragment-based inhibitor discovery to find a potential small-molecule-based inhibitor scaffold which may selectively bind at the NADPH binding site of SaTR. Our initial search using an internal library of small molecules suggests functionalized 2,3-dihydrofuro[3,2-c]dimedone as one of the plausible candidate scaffolds which may selectively bind at the NADPH binding cavity of SaTR to finally hinder the electron flow to bound FAD and subsequently to the substrate OxTrx (Figure S50).

2.2. Synthesis of 2,3-Dihydrofuro[3,2-c]dimedone Analogues.
Influenced by the initial results of virtual screening as well as the previously reported broad-range biological activity of dihydrofurans, we set out to synthesize diversely functionalized 2,3-dihydrofuro[3,2-c]dimedones in an eco-friendly manner to develop potential antagonistic leads against SaTR. Based on literature reports[19−21] and our ongoing interest in the development of multicomponent reactions[18,22,23] to find optimal catalytic conditions to synthesize 2,3-dihydrofuro[3,2-c]dimedones, we used a model substrate dimedone **1a**, 2-bromoacetophenone **1b**, and benzaldehyde **1c** along with a variety of catalysts and conditions to get 2,3-dihydrofuro[3,2-c]dimedone **1** (see Table 1). Initially, the model reaction performed in MeCN at 65 °C with the catalytic amounts of Ph$_3$P, Cu (OTf)$_2$, and *p*-TsOH failed to generate intended product **1** (see entries 1−3, Table 1). Moreover, the water-mediated taurine-catalyzed reaction failed to furnish the

Table 1. Optimization of Reaction Conditions

entry	catalyst	solvent	temp. (°C)	time (h)	yield (%)
1	Ph$_3$P	MeCN	65	24	
2	Cu (OTf)$_2$	MeCN	65	24	
3	p-TsOH	MeCN	65	24	
4	taurine	H$_2$O	80	24	
5	imidazole	MeCN	65	24	25
6	imidazole	H$_2$O	100	20	35
7	K$_2$CO$_3$	H$_2$O	100	12	9
8	DMAP	H$_2$O	100	12	12
9	Et$_3$N	H$_2$O	100	12	6
10	DABCO	H$_2$O	100	12	10
11[c]	imidazole	H$_2$O	100	8	88
12[d]	imidazole	H$_2$O	100	7	82

[a]Reactions were carried out in H$_2$O (5.0 mL) with 1.0 equiv of each substrate **1a** (0.713 mmol), **2a** (0.713 mmol), and **3a** (0.713 mmol) in the presence of 1.0 equiv of catalyst. [b]Yield refers to the column-purified product. [c]2.0 equiv of catalyst was used. [d]3.0 equiv of catalyst was used.
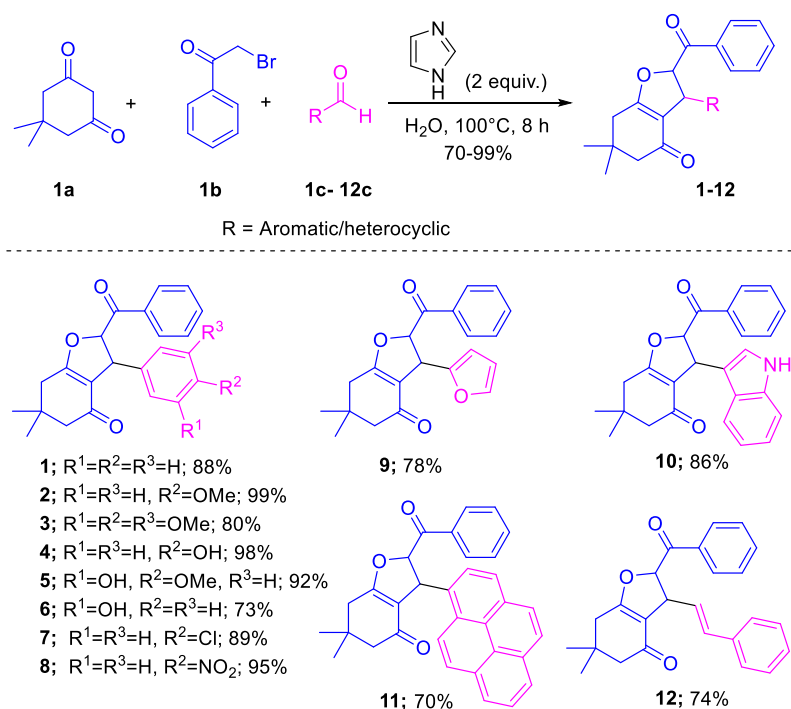
desired product at 80 °C after 24 h (entry 4, Table 1). However, the reaction of model substrate in the presence of imidazole (1.0 equiv) in MeCN at 65 °C produced the desired product **1** with 25% yield (entry 5, Table 1). Furthermore, keeping the imidazole intact at 100 °C in water resulted in a 35% yield in 20 h (entry 6, Table 1). At this juncture, numerous catalysts were screened, and their catalytic loading was varied in an effort to determine the optimal catalytic condition while maintaining water as a green solvent. Notably, the lead obtained by varying the catalyst from imidazole to K$_2$CO$_3$, DIMAP, Et$_3$N, and DABCO delivered the required products with trace or marginal yields along with the Knoevenagel adduct (entries 7–10, Table 1). Remarkably, catalyst loading from 1.0 equiv to 2.0 equiv in water afforded the desired product **1** with the highest 88% yield in 8 h (entry 11, Table 1). A further increase of the equivalent amount of the catalyst (imidazole; 3.0 equiv) delivered the desired product **1** in 7 h, with a reduced yield of 82% (entry 12, Table 1).

Hence, the optimal condition was confirmed with 2.0 equiv of imidazole in water at 100 °C that produced desired product **1** in 88% yield. Further, we appraised the breadth and scope of the developed approach by the reaction of dimedone **1a**, 2-bromoacetophenone **1b**, and aldehydes **1c−12c** to access multifunctionalized dihydrofuran analogues **1−12** (Scheme 2). Accordingly, the imidazole-catalyzed three-component reaction between dimedone **1a**, 2-bromoacetophenone **1b**, and diverse aldehydes **1c−12c** in water proceeded smoothly, furnishing the desired 2,3-dihydrofuro[3,2-c]dimedone (**1−12**) with an excellent yield of 70−99% (Scheme 2). The established approach was well tolerated by aromatic rings containing electron-donating substituents **2c−6c** and electron-withdrawing substituents **7c−8c**, yielding the corresponding products **2−8** in very high yields of 73−99% (Scheme 2).

Moreover, the developed approach was well operated even with the heterocyclic aldehydes such as furfural **9c** and indole-3-carboxaldehyde **10c** to produce **9** and **10** with 78 and 86% yield, respectively (Scheme 2). Interestingly, the reaction with polycyclic aldehyde (1-pyrenealdehyde) **11c** and cinnamaldehyde **12c** also underwent smoothly and produced novel derivatives of 2,3-dihydrofuro[3,2-c]dimedones **11** and **12** in 70 and 74% yield, respectively (Scheme 2). The structures of all of the newly synthesized 2,3-dihydrofuro[3,2-c]dimedones

Scheme 2. Synthesis of Dimedone-Fused 2,3-Dihydrofurans 1−12

R = Aromatic/heterocyclic

1; R^1=R^2=R^3=H; 88%
2; R^1=R^3=H, R^2=OMe; 99%
3; R^1=R^2=R^3=OMe; 80%
4; R^1=R^3=H, R^2=OH; 98%
5; R^1=OH, R^2=OMe, R^3=H; 92%
6; R^1=OH, R^2=R^3=H; 73%
7; R^1=R^3=H, R^2=Cl; 89%
8; R^1=R^3=H, R^2=NO$_2$; 95%

9; 78%

10; 86%

11; 70%

12; 74%

1−12 were derived from spectroscopic data (^{1}H and ^{13}C NMR, IR, and HRMS).

Looking into an excellent reactivity and mild reaction conditions, we further investigated the extent of the developed green approach to construct polyfunctionalized dihydrofurans **13−20** utilizing derivatives of 2-bromoacetophenone **2b** and **3b**. Intriguingly, the reaction of dimedone **1a** and aldehydes **1c/2c/6c/11c** with the derivatives of 2-bromoacetophenone **2b** (4-Br) and **3b** (4-OMe) proceeded very well to produce the designed analogues of 2,3-dihydrofuro[3,2-*c*]dimedones **13−20** with 70−96% yield (Scheme 3). The structures of all

Scheme 3. Synthesis of Dimedone-Fused 2,3-Dihydrofurans 13−20
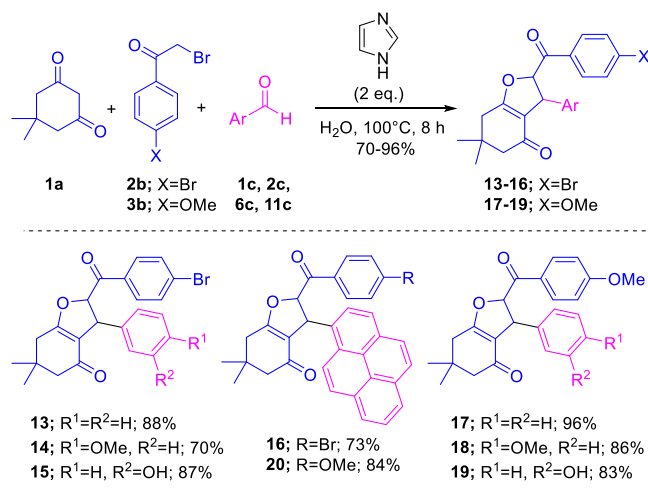
the lately synthesized 2,3-dihydrofuro[3,2-c]dimedones **13−20** were derived from spectroscopic data (^{1}H and ^{13}C NMR, IR, and HRMS). In our previous report,[22] we observed that the amphoteric nature of imidazole[24] plays a crucial role in our understanding of the mechanism. Initially, imidazole reacts with 2-bromoacetophenone to form an imidazolium ylide.[25] This ylide then undergoes nucleophilic attack on the Knoevenagel adduct, which is formed by the reaction of an aldehyde and dimedone, yielding the formation of the desired product.

2.3. Cloning, Overexpression, Large-Scale Protein Production, and Purification of the Target Proteins.

In order to determine if the synthesized DDHF has any in vitro SaTR inhibitory action, SaTR and its cognate substrate, Staphylococcal thioredoxin1 (SaTrx1), have been cloned (Figure S41) and overexpressed (Figure S42) in *Escherichia coli* M15 expression host (Qiagen Research). The sequence verified that targeted clones were further used for expression and purification of the corresponding proteins. SaTR and SaTrx1 were purified through immobilized metal affinity chromatography (IMAC) (using Ni-NTA resin), followed by gel filtration chromatographic techniques (Figure S43). Purified proteins were cryopreserved at −80 °C until used for further biochemical/kinetic assays.

2.4. SaTR Enzyme Inhibition Assay.

Intriguingly, the in silico experiments suggest that the majority of the synthesized DDHF derivatives stably bind at the NADPH binding site of SaTR with excellent free energy of binding profiles (Table ST1). However, in order to check the in vitro SaTR inhibition activities of synthesized DDHF derivatives, in vitro SaTR enzymatic activity was carried out using purified SaTR protein.

Cystine and the purified Staphylococcal thioredoxin 1 (SaTrx1) were separately used as the electron-accepting substrates of SaTR. For SaTR-mediated enzymatic reduction of cystine and oxidized SaTrx1, the rate of oxidation of the terminal electron donor, the labile SaTR cofactor NADPH to its oxidized form, NADP$^+$, was spectrophotometrically followed at 340 nm. Interestingly, among all the synthesized DDHF ligands, derivatives **5**, **8**, **16**, and **20** were found to exhibit SaTR inhibition activities at low to mid micromolar concentrations (in the range of 15−200 μM). As is evident in Figure 1A, among the all tested ligands, 2,3-dihydrofuro[3,2-*c*]dimedone derivative **20** (DDHF20) was found to exert the most potent SaTR inhibition in vitro which is corroborated by significant loss of NADPH oxidation rate in the presence of DDHF20 compared to the no inhibitor control. Henceforth, DDHF20 was further used to deduce in detail the kinetic mechanism of SaTR inhibition as well as to perform its anti-Staphylococcal activity and to divulge the structure-guided mechanistic details of SaTR inhibition.

Intriguingly, DDHF20 was found to inhibit the SaTR enzyme as a NADPH-competitive inhibitor. The double-reciprocal plot (Figure 1B) of SaTR-catalyzed NADPH oxidation carried out at different concentrations of cofactor NADPH and in three different concentrations of DDHF20 inhibitor clearly suggests the reduced affinity of cofactor NADPH to bind the free SaTR enzyme in the presence of increasing concentration of the inhibitor (signified by different slopes of enzyme-catalyzed reactions in the presence of increasing concentrations of the inhibitor). However, the maximum rate of NADPH oxidation in the presence of the inhibitor was found be unaltered in the presence of the inhibitor (as indicated by the common y axis intercept of the enzyme-catalyzed reactions in the presence of different concentrations of the inhibitor). Interestingly, the double-reciprocal plot of the SaTR-catalyzed NADPH oxidation reaction was found to deviate from linearity. The upward curvature of the double-reciprocal plot suggests that, in SaTR, NADPH binding follows a positive cooperative mode. Considering the obligate dimeric nature of SaTR enzyme (PDB: 4GCM), the positive cooperativity of NADPH binding may stem from two successive NADPH binding events, where NADPH binding to one SaTR monomer results in a structural change which increases the NADPH binding affinity to the second monomer. The deviation of linearity of the double-reciprocal plot hindered the determination of the K_i of the inhibitor, DDHF20. Hence, binding of DDHF20 to SaTR was further followed by the quenching of the intrinsic tryptophan fluorescence (Figure 1D).

Interestingly, the Stern−Volmer plot of DDHF20-mediated quenching of SaTR was also found to deviate from linearity, and once again, the upward curvature of the Stern−Volmer plot also suggests that, just like NADPH, DDHF20 binding to SaTR is also positively cooperative in nature. Compared with NADPH, the similar mode of the inhibitor DDHF20 binding to SaTR may also justify the commonality of their SaTR binding sites, as also indicated by the double-reciprocal plots mentioned earlier. The K_d value of DDHF20 to purified SaTR was found to be 69 μM. Once again, in SaTR, since the labile redox cofactor NADPH reduces the tightly bound prosthetic group FAD, therefore, the competitive displacement of NADPH by the inhibitor DDHF20 would also disrupt the NADPH-mediated FAD reduction mechanism. In order to test this phenomenon, NADPH-mediated reduction of FAD was
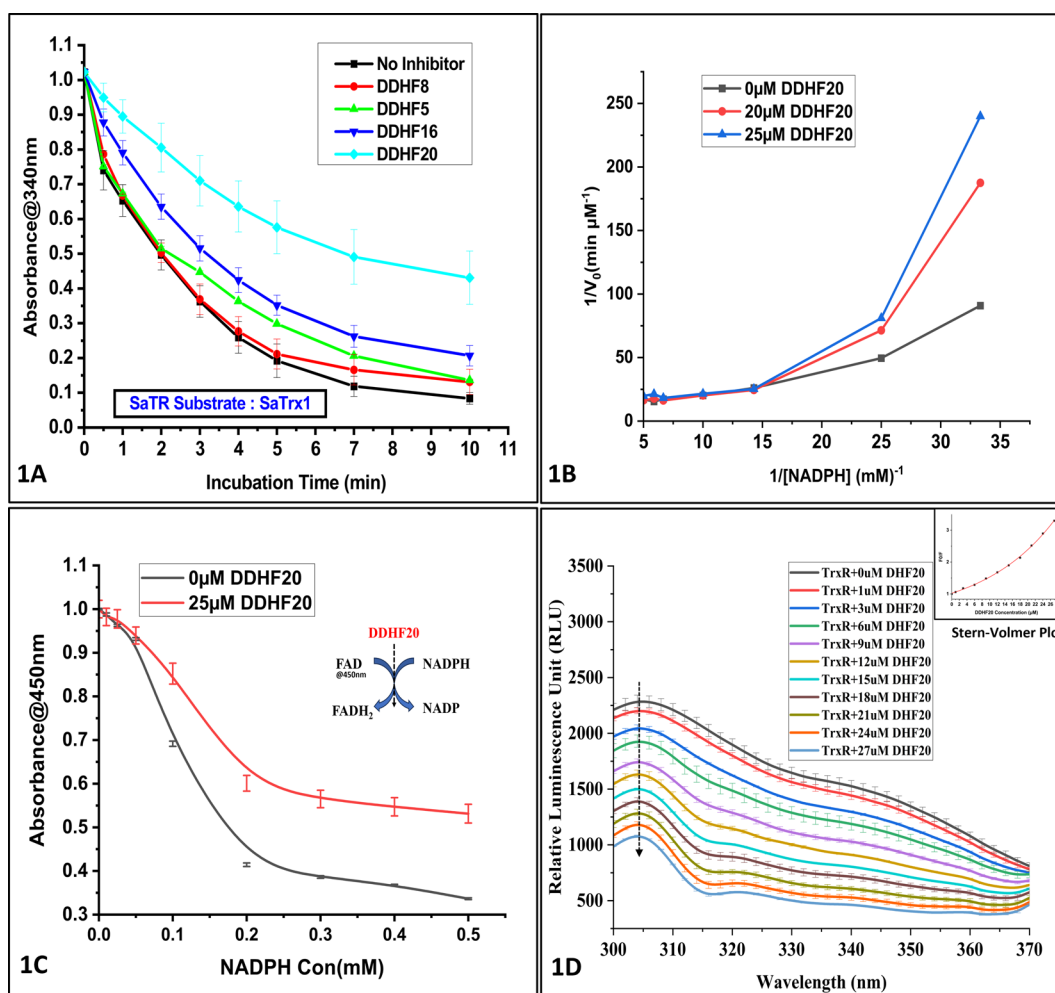
Figure 1. In vitro mechanistic details of SaTR inhibition activity of the DDHF derivatives: (A) in vitro screening of the SaTR inhibition activity of DDHF derivatives; the time course absorbance decreases at 340 nm because the oxidation of NADPH to NADP$^+$ in the presence and absence of DDHF derivatives (**5**, **8**, **16**, and **20**) reveals the inhibition of SaTR while using SaTrx1 as the electron-accepting substrate. (B) Lineweaver−Burk plot illustrating the kinetic mode of DDHF20 (the best inhibitor)-mediated inhibition of SaTR enzyme; DDHF20 competes for the NADPH binding site of the SaTR enzyme. (C) Redox conversions of the SaTR-bound prosthetic group FAD into FADH$_2$ as a function of increasing concentrations of NADPH in the presence and absence of DDHF20 inhibitor (monitored by reduction of FAD absorbance at 450 nm). NADPH-mediated electron donation to FAD is uncoupled in the presence of DDHF20 inhibitor. (D) Intrinsic tryptophan fluorescence quenching (monitored by reduction of tryptophan fluorescence emission maxima at 305 nm) as a result of DDHF20 binding with the SaTR enzyme. The inset shows the corresponding Stern−Volmer plot of fluorescence quenching (inset added in Figure S51 for a better view). The experiments have been performed in triplicates, and the mean values have been plotted along with the standard deviation. Error bar indicates standard deviation.

spectrophotometrically followed in the presence and absence of inhibitor DDHF20 in vitro. As expected, the reduction of the SaTR-bound FAD to FADH2 (followed by loss light absorption at 450 nm) as a function of increasing concentrations of NADPH was found to reduce significantly in the presence of DDHF20 inhibitor (Figure 1C).

2.5. Synthesis, Characterization, and Anti-Staphylococcal Activity of DDHF20-Capped Silver NPs. The antibacterial efficacy of DDHF20 was evaluated using *S. aureus* in the presence of induced oxidative stress; this led to a decrease in microbial survival to an extent of approximately 3-fold compared to that of the control (Figure S44). Despite the full spectrum of anti-Staphylococcal activity of DDHF20, in this test may be limited due to its lower solubility in aqueous buffer/media systems [which was also predicted in the in silico ADME screening (Figure S45)], considering this fact, we have synthesized DDHF20-capped silver NPs (DNPs) as the efficient delivery vehicle to increase its bioavailability. The

DNPs were further characterized for their size, monodispersity in aqueous buffer, and the presence of DDHF20 coating; these properties were also compared with those of the chemically synthesized bare silver NPs which were used as the precursor. Furthermore, the bactericidal property of the DNPs against *S. aureus* cells was also tested and compared with that of the chemically synthesized silver NPs.

Intriguingly, the UV−visible spectra of the plasmonic silver NPs, which are also indicative of their in-solution particle size, suggest that DNPs have higher hydrodynamic radii compared to the bare silver NPs. In contrast to the chemically synthesized bare silver NPs which show maximum UV−visible absorbance at 398 nm, the DNPs show maximum UV−visible absorbance at 418 nm (Figure 2A). The red shift of the UV−visible absorption maxima of the DNPs suggests their increased hydrodynamic radii compared to the chemically synthesized bare silver NP precursors, which may result from successful DDHF20 capping.
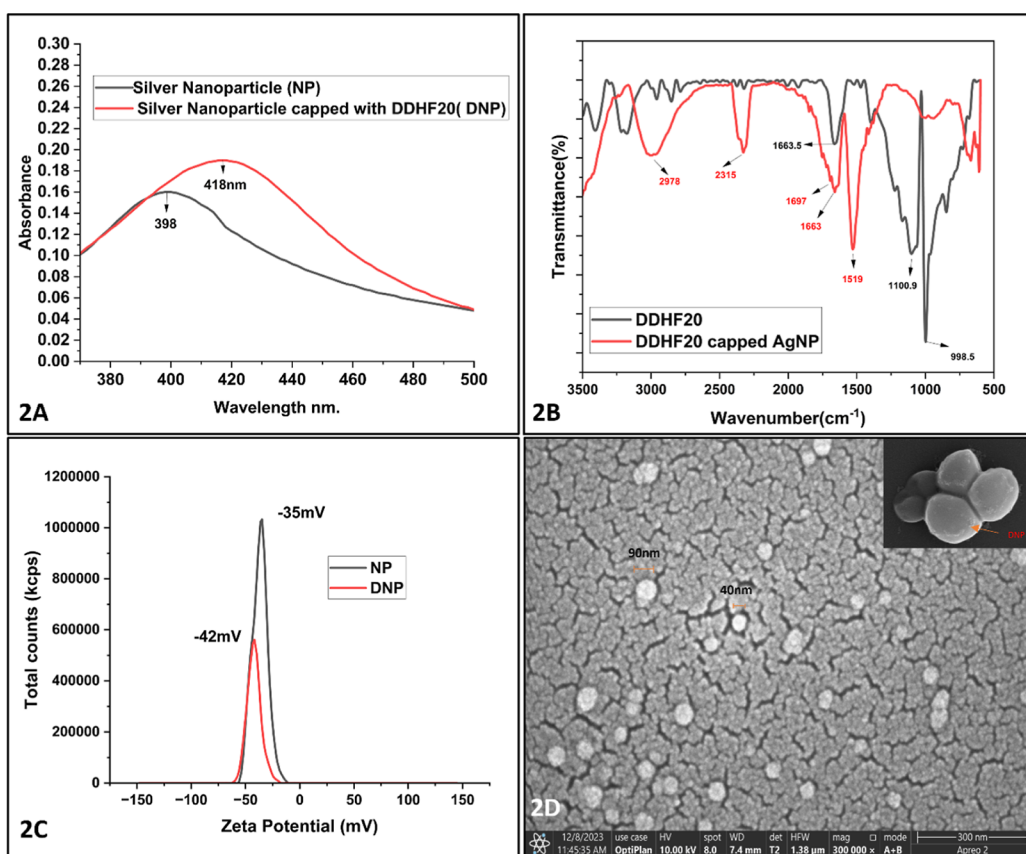
Figure 2. Characterization of DNPs: (A) comparison of absorption spectra of silver NPs and DNPs; the red-shifted absorption spectra of DNPs are suggestive of its increased hydrodynamic radii compared to the NP precursor. (B) FTIR spectra of a pure DDHF20 derivative and DNPs show the fingerprint vibrational stretching of different functional groups. (C) Comparison of the zeta potential of silver NP precursor and DNPs. (D) Field emission scanning electron microscopy image analysis of DNPs shows that the particles synthesized are in 40−100 nm range, and the inset shows the alteration of morphology of *S. aureus* cells after treatment with DNPs for 6 h (red arrow in the inset shows deposited DNPs on the *S. aureus* cell surface).

FTIR spectroscopy, which can delineate the surface chemistry of the synthesized NPs, was also performed to assess the successful capping of DDHF20 on silver NPs and compared with the purified DDHF20 molecule. The FTIR analysis can precisely assess the presence of the IR-active functional groups through the detection of fingerprint vibration spectra of a molecule. While comparing the FTIR spectra of the purified DDHF20 with DNPs, we found that the FTIR peaks corresponds to the vibrational stretching at 2978, 2315, 1697, 1663, 1519 cm^{-1}, etc. The C=C peak at 1663 cm^{-1} decreased while capping, confirming the capping of DDHF20 on silver NPs. The C=O, N−O, O=C=O, and C−H stretching can be evaluated with peaks at 1697, 1519, 2315, and 2978 cm^{-1} (Figure 2B).

Dynamic light scattering (DLS) was also performed to assess the hydrodynamic radii, in-solution polydispersity, as well as the zeta potential of the synthesized DNPs, and these properties were compared with those of the chemically synthesized bare silver NPs. The average hydrodynamic radii of the chemically synthesized bare silver NPs were found to be ~30 nm, whereas the average hydrodynamic radii of DNPs were found to be in the range of ~40−90 nm. The increased average hydrodynamic radii of the DNPs corroborate with the red-shifted UV−visible absorption maxima of these particles compared to the chemically synthesized bare silver NPs. Intriguingly, the zeta potential of bare silver NPs was found to be −35 mv; in contrast to that, DNPs elicited a zeta potential

of −42 mv (Figure 2C). The zeta potential values of DNPs indicate their stable nanosuspension. Once again, compared to the bare silver NPs, an increase in less negative zeta potential of DNPs is suggestive of their better in-solution stability (lesser aggregation), which may stem from successful DDHF20 capping.

2.6. In Vitro Antimicrobial Activity of DNPs. Drug-capped silver NPs have been previously found to elicit excellent drug delivery to the targeted cells or organs.[26] Herein, we tested the anti-Staphylococcal potency of the synthesized DNPs and compared the results with those of the uncapped (bare) silver NPs in vitro. Agar well diffusion assay shows that the DNPs have the potential to inhibit the growth of *S. aureus* with 1.76 ± 0.05 cm^2 of average zone of inhibition with 100 μg concentration of DNPs. In contrast, bare silver NPs have 0.78 ± 0.05 cm^2 of average zone of inhibition with 100 μg of NP concentration (Figure S46).

The minimum inhibitory concentration (MIC) value of DNPs against *S. aureus* ranges from 200 to 250 μg/mL, whereas using the same *S. aureus* strains, for bare silver NPs, the MIC value was found to be 300−375 μg/mL.

FESEM images of the *S. aureus* cells treated with DNPs clearly indicate the deposition of the NPs on the cell surface and the altered cell morphology (Figure 2D inset) which further culminates into cell lysis.

Intriguingly, bacterial thioredoxin reductases are well known to participate in the antibacterial defense mechanism against
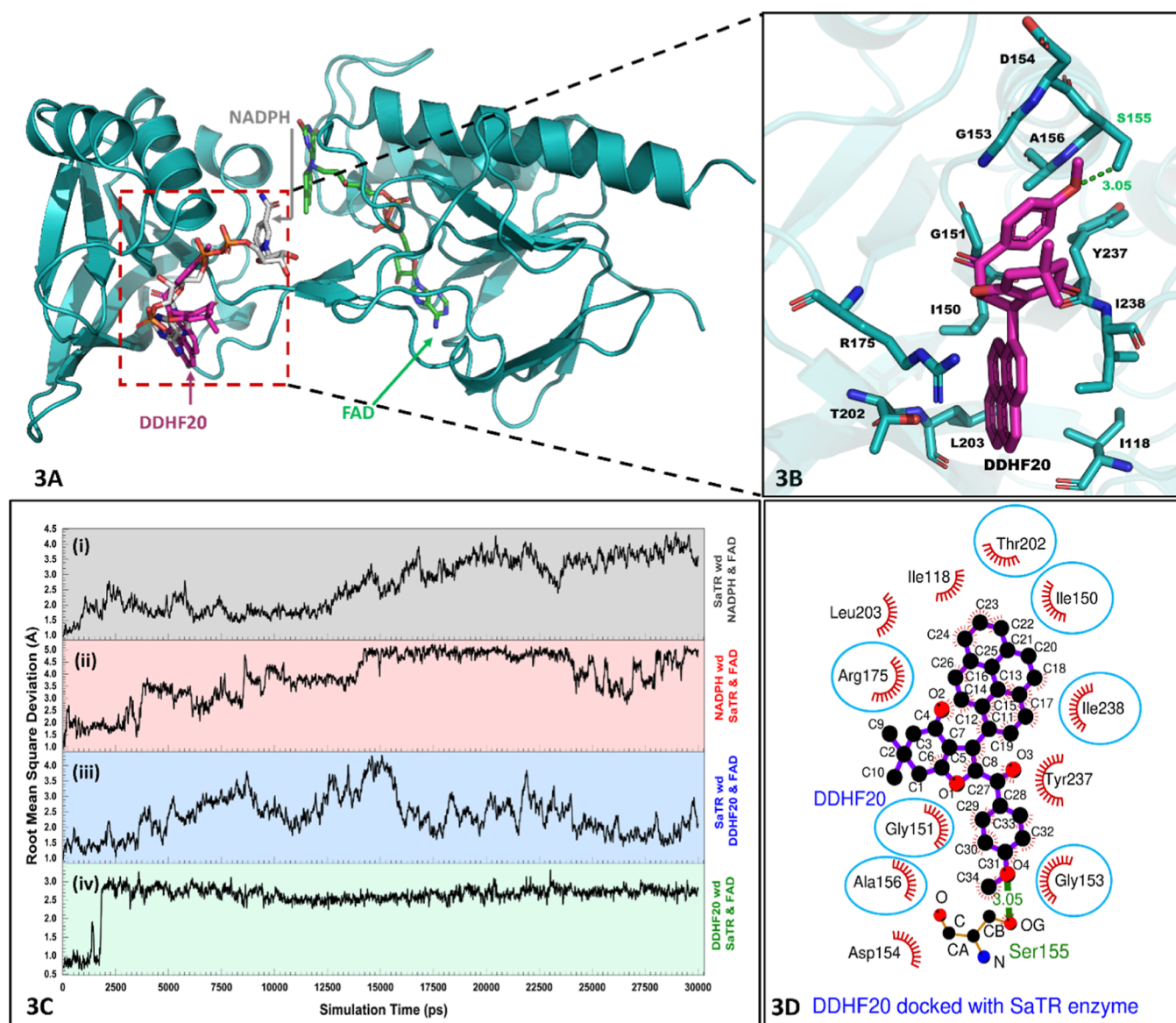
Figure 3. In silico binding interaction of DDHF20 with SaTR enzyme: (A) molecular docking of DDHF20 with SaTR shows that DDHF20 (represented by magenta sticks) binds at the NADPH (represented by silver sticks) binding pocket of SaTR. (B) Three-dimensional zoomed-in view of the DDHF20 interaction with the active site amino acid residues of the NADPH binding pocket of SaTR. Green dotted line represents the hydrogen bonding between S155 and DDHF20. (C) All atomistic MD simulation experiment generated by the RMSD profile of docked DDHF20 suggests that the bound DDHF20 is more stable than NADPH in the active site pocket during 30 ns simulation time period (as indicated by comparison of the red [SaTR-bound NADP] and green [SaTR-bound DDHF20] RMSD trace points). (D) 2D interaction profile of the docked DDHF20 at the NADPH binding pocket of SaTR; the blue circles show the common amino acid residues involved in the binding of DDHF20 and NADPH at the active site pocket. The red spiked arches indicate the hydrophobic interaction between the DDHF20 and the active site amino acid residues, while the formation of the hydrogen bond is indicated by the green dotted line.

ROS/RNS species which principally attack bacterial cell membrane through lipid peroxidation. Inhibition of thioredoxin reductase, therefore, may account for altered bacterial cell morphology due to impaired cell defense mechanisms to resist membrane lipid peroxidation, which would further culminate into cell death and lysis. Herein, the SaTR inhibitory activity of DDHF20 as observed in the biochemical studies may also corroborate with the superior anti-Staphylococcal activity of the synthesized DNPs.

2.6.1. Serum Stability of DNPs. We evaluated DNP serum stability since serum enzymes may render the drug ineffective or reduce its concentration over time. After incubating fetal bovine serum (FBS) 25% with DNP for 0, 2, 4, and 6 h, the

stability test showed no significant change in DNP MIC value after 4 h (Figure S47a). Moreover, characteristic fluorescence spectra of DNPs with FBS at different time points of incubation also indicates that there is no shift in DNP emission wavelength (i.e., 460 nm) even after 6 h of incubation with FBS (Figure S47b).

2.6.2. In Vitro Cell Line-Based Cytotoxicity Assay of DDHF20. Subsequently, we evaluated the cytotoxicity of DDHF20 in A549 cell lines using both dose- and time-dependent approaches. Even after 24 h of treatment with DDHF20, bright-field microscopy pictures revealed no detrimental effects on A549 cells, indicating the absence of

toxicity at 25, 50, and 100 μM concentration of the compound up to 24 h of incubation (Figure S48).

2.7. In Silico Study. In order to delineate the precise mechanistic details of DDHF20-mediated inhibition of SaTR, in silico docking followed by all atomistic molecular dynamics simulations was carried out. Targeted docking of the DDHF20 molecule at the highly conserved NADPH binding site of SaTR (Figure S49) resulted in tight binding of the ligand at the NADPH binding site, as evident by the excellent free energy of binding (−8.4 Kcal/mol) and the associated MM/PB(GB)SA score (−17.68 kcal/mol). The stability of the DDHF20-SaTR/FAD complex was also assessed through all atomistic MD simulation studies and was also compared with the stability of the NADPH-SaTR/FAD complex. Intriguingly, the RMSD fluctuations of the DDHF20 ligand in its SaTR (FAD)-bound form were found to be more stable compared to the redox cofactor NADPH in its SaTR/FAD-bound form during the all-atomistic MD simulation time trajectory (30 ns) (Figure 3C). The strong and stable binding of DDHF20 at the NADPH binding site of SaTR is exemplified by the formation of a good number of hydrophobic interactions with the amino acid residues at the NADPH binding pocket of SaTR (Figure 3A,B). The 2D interaction plot (Figure 3D) shows that NADPH and DDHF20 share seven common interacting amino acid residues at the SaTR binding pocket. However, unlike redox cofactor NADPH, the synthesized ligand, DDHF20, lacks the electron-donating nicotinamide ring; hence, it cannot interact with the isoalloxazine ring of the bound FAD. The involvement of identical sets of interacting amino acid residues in DDHF20 and NADPH binding, as well as the predicted stable binding of DDHF20 at the NADPH binding site of SaTR, further justifies the competitive mode of inhibition exerted by DDHF20 in context of NADPH binding. The binding of DDHF20 in the NADPH binding pocket may hinder the relay of electrons from NADPH to FAD to the final active site cystine residues of oxidized SaTR. This uncoupling of the electron relay system will disable the crucial antioxidative defense mechanism of *S. aureus* resulting in bacterial death under oxidative stress. However, high-resolution crystal structure of the DDHF20-SaTR/FAD complex is further sought to shed light on the precise molecular mechanism of action of the inhibitor.

3. CONCLUSIONS

The antibiotic-resistant *S. aureus* strains are becoming the major problem in the global healthcare sectors, and novel therapeutic leads or scaffolds are urgently needed to combat this pathogen. Herein, in search for a novel inhibitor scaffold against a well-established anti-Staphylococcal drug target enzyme, thioredoxin reductase (SaTR), we have developed an imidazole-catalyzed water-mediated green multicomponent approach for the synthesis of dimedone-coupled 2,3-dihydrofuran (DDHF) derivatives, utilizing widely accessible dimedone, aromatic/heterocyclic/polycyclic aldehydes/cinnamaldehyde, and 2-bromoacetophenone with derivatives. Water-mediated mild reaction conditions and reactivity of the imidazole catalyst system toward a wide range of aromatic aldehydes provided access to a range of densely substituted cum highly functionalized DDHF derivatives in excellent yields. The synthesized DDHF derivatives have been found to inhibit purified SaTR enzyme at low to mid micromolar concentration ranges in vitro. Furthermore, detailed in vitro enzyme kinetic analysis of the best DDHF derivative inhibitor,

DDHF20 ($K_d \sim 69\ \mu$M), demonstrated its capability to compete with the SaTR's redox-active labile cofactor, NADPH, and thereby can uncouple the NADPH-FAD electron-transfer reaction. In silico docking and all atomistic MD simulation results also suggest strong and stable binding of DDHF20 at the highly conserved NADPH binding pocket of SaTR. SaTR is the crucial enzyme needed to combat reactive oxygen species (ROS) stress-related cellular damages in *S. aureus*. NADPH acts as the labile redox cofactor of SaTR to carry out its antioxidative defense mechanism. Hence, by virtue of competing for the NADPH binding site of SaTR, DDHF20 can effectively inhibit the enzyme's function and thereby subsequently inhibit the antioxidative defense mechanism of *S. aureus*. In this context, DDHF20 was also found to kill ROS-stressed *S. aureus* cells in vitro. Furthermore, in contrast to the bare silver NPs, synthesized DNPs were found to exhibit excellent anti-Staphylococcal activity in vitro (MIC 200−250 μg/mL). Once again, the in vitro cellular cytotoxicity assay as well as the serum stability analysis of DDHF20 also infer its suitability as a potential future therapeutic lead. Altogether, the in vitro and in silico SaTR inhibition activity as well as the anti-Staphylococcal properties of DDHF20 presented hitherto may indicate that the synthesized DDHF scaffold holds immense promise to yield potent anti-Staphylococcal therapeutic leads in the future, through pharmacophore-mediated rational drug designing approaches.

4. MATERIALS AND METHODS

All the in vitro reactions have been performed in triplicate, and standard deviation has been calculated for all the data plotted. The reagents used in the study have been purchased from Sigma-Aldrich, HiMedia, and SRL. In silico studies have been performed with System with Intel Xenon W-2275 CPU, 4GB RAM with NVIDIA graphics, and Ubuntu Operating system. The dimedone-fused 2,3-dihydrofuran has been abbreviated as DDHF.

4.1. Structure-Guided Fragment-Based Pharmacophore Modeling. The crystal structure of thioredoxin reductase from *S. aureus* (PDB id: 4GCM) has been used in the study and protein prepared with Auto Dock Vina tools and was energy-minimized with Phenix.[27] The fragment library was prepared based on the NADPH binding site, and a virtual docking study has been performed with modeled ligands. The modeled structures have been synthesized.

4.2. Pharmacophore Synthesis. All reactions were performed in standard glassware with no special precautions taken for the exclusion of moisture or air unless otherwise mentioned. All reagents were of reagent-grade quality, purchased commercially from Sigma-Aldrich and Avara, and used without further purification. Products were purified by column chromatography on 250−400 mesh silica gel using ethyl acetate (EtOAc) and hexane. Thin-layer chromatography (TLC) analyses were performed using 0.25 mm Merck silica gel plates 60 F254, checked by UV light, and stained with anisaldehyde stain.

NMR spectra were recorded on a Bruker High Performance Digital FT-NMR (Model: AVANCE III HD, Ascend TM WB, 500 MHz Equipment control: Topspin 3.2 Features Standard operating procedure) and Bruker ALPHA (Eco-ATR) spectrometer by using CDCl$_3$ as a solvent and TMS is the internal reference. The HRMS data were collected using a 6545 LC/Q-TOF HRMS.

The following abbreviations were used to explain the multiplicities: s = singlet, d = doublet, t = triplet, q = quartet, dd = doublet of doublet, ddd = doublet of a doublet of a doublet, dt = doublet of a triplet, m = multiplet, and br = broad.

A mixture of dimedone **1a** (0.713 mmol) and aldehyde **1c**–**12c** (0.713 mmol) in 5 mL of water was stirred at 100 °C for 10 min. Subsequently, 2-bromoacetophenone **1b**–**3b** (0.713 mmol) and imidazole (1.426 mmol) were added, and the mixture was stirred at 100 °C for 8 h. The reaction was analyzed using TLC, and after completion of the reaction, the reaction mixture was cooled to room temperature, and the product was extracted with EtOAc (2 × 10 mL). The organic layer was dried over anhydrous Na_2SO_4, and the solvent was removed on a rotavapor under reduced pressure and purified by silica gel chromatography using EtOAc/hexane mixture to obtain the desired product. General procedure for the synthesis of compounds has been given in the Supporting Information.

4.3. Cloning, Overexpression, Large-Scale Protein Production, and Purification of the Target Proteins. The *S. aureus* open reading frame of the target gene construct, i.e., SaTrxR (SAOUHSC_00785) and SaTrx1 (SAOUHSC_01100), was PCR-amplified with the corresponding forward and reverse primers, and the gene construct was from *S. aureus* RN4220 strain. The purified PCR product and PQE30 vector were subjected to restriction digestion and ligation. The ligated construct then transformed to *E. coli* DH5α-competent cells, and the positive colonies obtained after transformation were streaked on separate LB plates. The colony PCR was performed to check the presence of the desired clone by using gene specific primers. The recombinant DNA from the positive clones was purified and then transformed into expression host *E. coli* M15 cells. The recombinant protein expression was performed by growing the transformed *E. coli* M15 cells overnight with the ampicillin antibiotic. The concentration of IPTG for induction, post-induction incubation temperature, and hours were optimized. After induction, the cells were subjected to lysis and the protein expression checked with 12% SDS PAGE electrophoresis with a protein ladder by comparing it with an uninduced sample. After getting the overexpressed protein bands on SDS PAGE, we further moved for large-scale production of protein. For large-scale protein production and purification, several factors were optimized like IPTG concentration, postinduction incubation temperature and time, buffer, and its pH. The 2 L LB was inoculated with 10 mL overnight bacterial culture, and after 0.6 OD_{600} IPTG induction was given, the lysed cell culture was then subjected to centrifugation, and further supernatant was applied to the IMAC column. The buffer having Tris, NaCl, and different imidazole concentration was given, and the most purified fraction was collected and concentrated. The size exclusion chromatography was also performed to get the homogeneous purified protein fractions.

4.4. Thioredoxin Reductase Enzyme Inhibition Assay. Enzyme inhibition assay was performed with a Shimadzu 1900i UV−vis spectrophotometer at room temperature. Experiments were performed with Trx1 as well as with L-cystine (data not shown here) as a substrate. In the experiment where L cysteine acted as a substrate, the reaction mixture was prepared in the absence and presence of 2,3-dihydrofurans derivatives. In the control experiment, the reaction buffer, substrate L-cystine (150 μM), NADPH (0.2 mM), and SaTR enzyme (3 μM)

were added in sequence and mixed properly. The absorption at 340 nm was taken from 0 to 10 min. In the test sample, DDHF dissolved in dimethyl sulfoxide (DMSO) was added in micromolar concentration before the enzyme and rest conditions were the same. Throughout the experiment, the DMSO percentage was not higher than 1%. Similarly, in the second experiment having Trx1 as a substrate, first reaction buffer, NADPH (0.2 mM), enzyme SaTR (3 μM), insulin, and SaTrx1 (10 μM), was added in a sequence and mixed properly in the control reaction mixture. While in the test mixture, DDHF was added in micromolar concentration before the addition of insulin. We also performed assay where DTNB was working as a substrate using the modified protocol developed by Holmgren et al.[28] (data not shown here). In the control reaction mixture, reaction buffer, substrate DTNB (1 mM), NADPH (0.2 mM), and the last enzyme SaTR (3 μM) were added in sequence and mixed properly. The absorbance at 412 nm was taken from 0 to 10 min. In the same way, the reaction mixture was prepared where DDHF was added with all reagents before the enzyme addition.

4.4.1. Mode of Inhibition Study. To study the mode of inhibition, NADPH titration has been performed in the presence of different concentrations of DDHF20. In the reaction mixture, enzyme SaTR (3 μM) has been added, followed by NADPH (20, 30, 40, 70, 100, 150, 170, and 200 μM) and DDHF20 (0, 20, and 25 μM); the mixture was kept for 2 min incubation, then substrate L-cystine (150 μM) was added, and reading was taken quickly at 340 nm with a UV−vis spectrophotometer from 0 to 10 min.

4.4.2. NADPH Titration Study. The assay was performed with different concentrations of NADPH in the presence and absence of DDHF20. In the control experiment, SaTR was added first followed by NADPH, and absorbance scan was taken from 200 to 600 nm. In the test sample, there was addition of DDHF20 also.

4.4.3. Fluorescence Study. To study the in vitro binding profile of DDHF20 with purified Staphylococcal TrxR, we performed the in vitro fluorescence-based assay. The assay was performed using a quartz cuvette of 1 mL on a spectrofluorometer (JASCO FP8300). All the experiments were performed in triplicate. Protocols in brief, the TrxR final concentration in the reaction mixture was kept 2 μM throughout the whole experimentation. First of all, DDHF20 ligand was dissolved in 100% DMSO, and the final concentration of DMSO in the final reaction mixture was kept 1% by diluting with the same buffer. Varying DDHF20 concentrations like 1, 3, 6, 9, 12, 15, 18, 21, 24, and 27 μM were used for the interaction study. The final reaction mixture contains SaTrxR, varying concentration of ligand, 1% DMSO, and 1× reaction buffer up to 1 mL. Technical parameters for measurements like excitation and emission bandwidth were fixed 5 and 10 nm, respectively, sensitivity medium, response time 0.2 s, and scan speed 200 nm min^{-1}. The fluorescence emission spectra were recorded from 300 to 700 nm by exciting at 280 nm. The results of fluorescence spectra against ligand concentration were plotted using Origin software.

4.5. Preparation and Characterization of DNPs. The ADME properties of the ligand have been checked with the SwissADME[29] online tool, and due to less solubility and bioavailability, silver NPs have been synthesized and capped with the best ligand found in in vitro screening. Silver NPs have been synthesized by the method developed by Agnihotri et al.[30] with some modifications, for taking it as a positive

control in the study. Freshly prepared $AgNO_3$ dissolved in deionized water, kept at a hot plate magnetic stirrer at 70 °C and 200 rpm, and freshly prepared sodium borohydride as a reducing agent were added dropwise, and the appearance of a yellow color indicates the synthesis of silver NPs. To prepare the DNP, DDHF20 dissolved in methanol (0.2 mM) used as a reducing agent was added dropwise in $AgNO_3$ solution, and then sodium borohydride was added in the same manner. The UV−vis spectroscopic spectral analysis method was used to characterize the synthesized NP.

Capping of DDHF20 on silver NPs was confirmed with different biophysical techniques. The surface plasmon resonance absorption band recorded with UV−vis spectroscopy (Shimadzu UV Vis 1900i) with 2 nm resolution and peak shifting has been observed with capped DNP when scanned from 200 to 600 nm range. DLS (Malvern Zetasizer) has been used to predict the average particle size (hydrodynamic diameter) at 25 °C and zeta potential of the prepared silver NPs as well as DNPs. FTIR spectra have also been scanned from 500 to 3500 wavelength number to check the different functional groups present in DDHF20 and DDHF20-capped NP. The field emission scanning electron microscopy image analysis was also performed with Thermo Fisher Apero 2.

4.6. In Vitro Antimicrobial Study.
The DDHF20 antimicrobial activity in the presence of oxidative stress was evaluated by the assay developed by Sahu et al.[31] with some modifications. The S. aureus culture was cultivated until it reached an optical density of 0.4 OD600. Subsequently, the culture was exposed to DDHF20 (25 μM). After a 30 min incubation period, reactive oxidative stress was induced using tertiary butyl hydroperoxide (10 mM). Then, 5 μL of various treated serially diluted samples were applied to an agar plate. The colony was counted after a duration of 16 h. The culture was treated as a control in the absence of DDHF20.

The antimicrobial activity of DNPs has been tested for their antimicrobial activity with the method developed by Kirby−Bauer[32] with some modifications. The *S. aureus* bacterial culture has been grown, and its suspension was spread evenly on an agar plate using sterile swab. The control (silver NPs prepared with sodium borohydride) and the test (silver NPs prepared with DDHF20) sample have been poured in the wells formed, and the plate was kept overnight at 37 °C. The zone of inhibition has been measured.

The MIC of DNPs and NPs has also been calculated with a microtiter well broth dilution method as was used by Jaiswal et al.[33] S. aureus inoculum without DNPs/NPs was taken as a negative control, and nutrient broth alone was taken as a positive control. The 375−0.2 μg/mL concentration of NPs/DNPs has been tested. Each well of a 96-well microtiter plate was filled with 100 μL of nutrient broth, 2 μL of inoculum, and 98 μL of NPs/DNPs, followed by serial dilution. After 24 h of incubation at 37 °C, absorbance was taken at 600 nm from a plate reader. All the experiments were performed in triplicate.

4.6.1. Serum Stability Assay.
The serum stability of DNPs was determined by the method used by Guo et al.[34] with some modifications. DNPs were added to 25% FBS, and MIC was evaluated at 0, 2, 4, and 6 h of incubation of DNPs with FBS. The MIC study protocol was followed as earlier. The DNP stability in FBS was assessed by comparing the MIC value of DNPs at different hours of incubation in FBS. In addition, the fluorescence study has been performed where the DNP was excited at 250 nm wavelength, and it was showing emission at

460 nm. After incubation with FBS, a fluorescence study at different incubation times has been observed.

4.6.2. Cell Viability Assay with DDHF20.
The A549 cells were exposed to different concentrations of DDHF20 (25, 50, and 100 μM) for 24 h. Additionally, at 6, 12, and 24 h time intervals, the cells were treated with a concentration of 50 μM of DDHF20. The control contains DMSO instead of DDHF20. The photos were captured by using a bright-field microscope (FLoid Cell Imaging Station).

4.7. In Silico Study.
4.7.1. Docking Study of SaTR with DDHF.
The 2,3-dihydrofuran (DDHF) derivatives with 2D structure were drawn with ChemDraw and further converted into 3D structure with the Open Bable[35] software. The SaTR non-twisted confirmation (PDB Id:4GCM) attached with cofactor FAD has been simulated with nanoscale molecular dynamics (NAMD) 2.14 software for 30 ns. The simulated structure was used for docking to remove all of the constrains. The receptor protein SaTR and ligands were prepared with AutoDock Tools[36] 1.5.6 for docking. While preparing the receptor protein, water was removed, and polar hydrogens and Kollman charges were added. The grid box was set for 1 Å spacing with 24 × 20 × 18 Å axes x, y, z, respectively, to target the ligand on the NADPH binding site. The ligand was docked with receptor protein, and with AutoDock Tools, we got ligand and protein binding affinity scores. The 2,3-dihydrofuran core structure was docked in a targeted manner with receptor protein (Figure S50). With AutoDock Tools, we got ligand and protein binding affinity scores, but to check the near-native binding pose affinity scores, we used the farPPI[37] server also, which uses the MM/PB(GB)SA[38] method for rescoring the docking poses of the ligand with the receptor. The server uses the GAFF2 force field for ligand, ff14SB force field for the receptor, and the PB3 procedure for rescoring the binding affinity. In this platform, we uploaded our mol2 file format of docked pose of interest of DDHF derivatives and the pdb file of the receptor protein. The server uses the input mol2 ligand file and generates each pose with AM1-BCC partial charges. Further, it generates the inpcrd and prmtop files with reciprocal radii of the ligand receptor complex. It also minimizes the complex with explicit solvent and generates rst files. At the final step, it generates the scores for docking poses with the MM/PB(GB)SA method.

4.7.2. Simulation Study of SaTR with DDHF.
To evaluate the results of the docking study and to check the behavior of ligands under different physiological conditions, simulation studies were performed with the NAMD 2.14 simulation platform. NAMD,[39] a molecular graphics program, employs visual molecular dynamics[40] for the file preparation. The Charmm-Gui Ligand Reader and Modeler[41] was used to get the parameter and trajectory files for the ligands. Solvation cubic of 10 Å was set with the isothermal−isobaric ensemble (NPT) environment with the help of Langevin dynamics. In the multiple time stepping conditions, time steps were kept 1 fs and 1 steps per cycle. The dcd, xst, restart frequencies, and output energies were set to 5000. Minimization was performed for 1000 steps before the simulation. SaTR with FAD and SaTR with FAD and NADPH analogue as well as SaTR with FAD and DDHF20 were simulated for 30 ns. Conserved site has been analyzed with Consurf[42] server using the pdb file of the receptor protein. The server color codes the conserved and variable regions.

■ ASSOCIATED CONTENT

ⓈⒾ Supporting Information

The Supporting Information is available free of charge at https://pubs.acs.org/doi/10.1021/acsomega.4c04325.

General procedure for the synthesis of DDHF, ^{1}H and ^{13}C NMR spectra, docking analysis, protein production, ADME profile, conserved sequence analysis, ZOI from DNPs and NPs, serum stability, and cell viability assay (PDF)

■ AUTHOR INFORMATION

Corresponding Authors

Rohan D. Erande − *Department of Chemistry, Indian Institute of Technology, Jodhpur 342037 Rajasthan, India;* ⓞ orcid.org/0000-0002-8763-5353; Email: rd.erande@iitj.ac.in

Sudipta Bhattacharyya − *Department of Bioscience & Bioengineering, Indian Institute of Technology, Jodhpur 342037 Rajasthan, India;* Email: sudipta@iitj.ac.in

Authors

Manjari Shukla − *Department of Bioscience & Bioengineering, Indian Institute of Technology, Jodhpur 342037 Rajasthan, India;* ⓞ orcid.org/0000-0002-5033-6683

Ghanshyam Mali − *Department of Chemistry, Indian Institute of Technology, Jodhpur 342037 Rajasthan, India*

Supriya Sharma − *Department of Chemistry, Indian Institute of Technology, Jodhpur 342037 Rajasthan, India*

Sushobhan Maji − *Department of Bioscience & Bioengineering, Indian Institute of Technology, Jodhpur 342037 Rajasthan, India*

Vinay Kumar Yadav − *Department of Bioscience & Bioengineering, Indian Institute of Technology, Jodhpur 342037 Rajasthan, India*

Amit Mishra − *Department of Bioscience & Bioengineering, Indian Institute of Technology, Jodhpur 342037 Rajasthan, India;* ⓞ orcid.org/0000-0001-9401-4400

Complete contact information is available at:
https://pubs.acs.org/10.1021/acsomega.4c04325

Author Contributions

All the authors contributed equally to this work.

Notes

The authors declare no competing financial interest.

■ ACKNOWLEDGMENTS

■ REFERENCES

(1) Foster, T. J. Antibiotic resistance in Staphylococcus aureus. Current status and future prospects. *FEMS Microbiol. Rev.* **2017**, *41* (3), 430−449.

(2) Chand, U.; Priyambada, P.; Kushawaha, P. K. Staphylococcus aureus vaccine strategy: Promise and challenges. *Microbiol. Res.* **2023**, *271*, 127362.

(3) Vestergaard, M.; Frees, D.; Ingmer, H. Antibiotic Resistance and the MRSA Problem. *Microbiol. Spectrum* **2019**, *7* (2), 10.1128/microbiolspec.gpp1123-0057-2018.

(4) Felix, L.; Mylonakis, E.; Fuchs, B. B. Thioredoxin Reductase Is a Valid Target for Antimicrobial Therapeutic Development Against Gram-Positive Bacteria. *Front. Microbiol.* **2021**, *12*, 663481.

(5) Dong, C.; Zhou, J.; Wang, P.; Li, T.; Zhao, Y.; Ren, X.; Lu, J.; Wang, J.; Holmgren, A.; Zou, L. Topical Therapeutic Efficacy of Ebselen Against Multidrug-Resistant Staphylococcus aureus LT-1 Targeting Thioredoxin Reductase. *Front. Microbiol.* **2020**, *10*, 3016.

(6) Lu, J.; Holmgren, A. The thioredoxin antioxidant system. *Free Radicals Biol. Med.* **2014**, *66*, 75−87.

(7) Lennon, B. W.; Williams, C. H., Jr.; Ludwig, M. L. Twists in catalysis: alternating conformations of Escherichia coli thioredoxin reductase. *Science* **2000**, *289* (5482), 1190−1194.

(8) Jacques, R.; Pal, R.; Parker, N. A.; Sear, C. E.; Smith, P. W.; Ribaucourt, A.; Hodgson, D. M. Recent applications in natural product synthesis of dihydrofuran and -pyran formation by ring-closing alkene metathesis. *Org. Biomol. Chem.* **2016**, *14* (25), 5875−5893.

(9) Kilroy, T. G.; O'Sullivan, T. P.; Guiry, P. J. Synthesis of Dihydrofurans Substituted in the 2-Position. *Eur. J. Org Chem.* **2005**, *2005*, 4929−4949.

(10) Madar, J. M.; Shastri, L. A.; Shastri, S. L.; Holiyachi, M.; Naik, N. S.; Shaikh, F.; Kumbar, V. M.; Bhat, K. G.; Joshi, S. D.; Sungar, V. A. The anti-inflammatory Design, Synthesis and Exploiting Pharmacological Activities of 2,3-Dihydrofuranocoumarins as Multi-Therapeutic Agents. *ChemistrySelect* **2018**, *3* (38), 10738−10749.

(11) Kashanna, J.; Kumar, R. A.; Kishore, R.; Kumar, D. N.; Kumar, A. S. 2,3-Dihydrofurans as Potential Cytotoxic and Antibacterial Agents: Tandem Knoevenagel-Michael Cyclization for the Synthesis of 2,3-Dihydrofurans by Using α-Tosyloxy Ketone Precursors. *Chem. Biodiversity* **2018**, *15* (11), No. e1800277.

(12) Ramesh, K. B.; Pasha, M. A. Study on one-pot four-component synthesis of 9-aryl-hexahydro-acridine-1,8-diones using SiO2-I as a new heterogeneous catalyst and their anticancer activity. *Bioorg. Med. Chem. Lett.* **2014**, *24* (16), 3907−3913.

(13) Montes-Avila, J.; Delgado-Vargas, F.; Díaz-Camacho, S. P.; Rivero, I. A. Microwave-assisted synthesis of hydropyridines and study of the DPPH-scavenging activity. *RSC Adv.* **2012**, *2* (5), 1827−1834.

(14) Khanam, H.; Shamsuzzaman. Bioactive Benzofuran derivatives: A review. *Eur. J. Med. Chem.* **2015**, *97*, 483−504.

(15) Martínez-Richa, A.; Mendoza-Díaz, G.; Joseph-Nathan, P. Keto-Enol Tautomerism of Dimedone Studied by Dynamic NMR. *Appl. Spectrosc.* **1996**, *50* (11), 1408−1412.

(16) Ma, G.-H.; Tu, X.-J.; Ning, Y.; Jiang, B.; Tu, S.-J. Efficient Domino Strategy for the Synthesis of Polyfunctionalized Benzofuran-4(5H)-ones and Cinnoline-4-carboxamides. *ACS Comb. Sci.* **2014**, *16* (6), 281−286.

(17) Findik, E.; Dingil, A.; Karaman, I.; Budak, Y.; Ceylan, M. Synthesis of Multi-substituted 4,5-Dihydrofuran Derivatives from (S)-Limonene and 1,3-Dicarbonyl Compounds and their Biological Activities. *E-J. Chem.* **2009**, *6*, 353268.

(18) Chavan, K. A.; Shukla, M.; Chauhan, A. N. S.; Maji, S.; Mali, G.; Bhattacharyya, S.; Erande, R. D. Effective Synthesis and Biological Evaluation of Natural and Designed Bis(indolyl)methanes via Taurine-Catalyzed Green Approach. *ACS Omega* **2022**, *7*, 10438−10446.

(19) Chuang, C.-P.; Chen, K. P. N-Phenacylpyridinium bromides in the one-pot synthesis of 2,3-dihydrofurans. *Tetrahedron* **2012**, *68*, 1401−1406.

(20) Wang, Q.-F.; Hou, H.; Hui, L.; Yan, C.-G. Diastereoselective Synthesis of trans-2,3-Dihydrofurans with Pyridinium Ylide Assisted Tandem Reaction. *J. Org. Chem.* **2009**, *74* (19), 7403−7406.

(21) Adib, M.; Rajai-Daryasarei, S.; Pashazadeh, R.; Jahani, M.; Yazzaf, R.; Amanlou, M. A Consecutive Four-Component Synthesis of

Polysubstituted Thiophenes in Aqueous Medium. *Eur. J. Org Chem.* **2018**, *2018* (23), 3001−3016.

(22) Mali, G.; Maji, S.; Chavan, K. A.; Shukla, M.; Kumar, M.; Bhattacharyya, S.; Erande, R. D. Effective Synthesis and Biological Evaluation of Functionalized 2,3-Dihydrofuro[3,2-c]coumarins via an Imidazole-Catalyzed Green Multicomponent Approach. *ACS Omega* **2022**, *7* (40), 36028−36036.

(23) Shaikh, S. M.; Yadav, V. K.; Mali, G.; Bondle, G. M.; Kumar, A.; Erande, R. D.; Bhattacharyya, S.; Bhosle, M. R. Convenient multicomponent synthesis of furo[3,2-c]coumarins in the promoting medium DIPEAc and assessment of their therapeutic potential through in silico pharmacophore based target screening. *New J. Chem.* **2022**, *46*, 22353−22362.

(24) Yamada, M.; Honma, I. Anhydrous proton conducting polymer electrolytes based on poly(vinylphosphonic acid)-heterocycle composite material. *Polymer* **2005**, *46* (9), 2986−2992.

(25) Glushkov, V. A.; Valieva, M. S.; Maiorova, O. A.; Baigacheva, E. V.; Gorbunov, A. A. N-heterocyclic carbenes: III. N-heterocyclic carbene ligands based on abietane in Suzuki-Miyaura reaction. *Russ. J. Org. Chem.* **2011**, *47* (2), 230−235.

(26) Nemčeková, K.; Svitková, V.; Sochr, J.; Gemeiner, P.; Labuda, J. Gallic acid-coated silver nanoparticles as perspective drug nanocarriers: bioanalytical study. *Anal. Bioanal. Chem.* **2022**, *414* (18), 5493−5505.

(27) Liebschner, D.; Afonine, P. V.; Baker, M. L.; Bunkóczi, G.; Chen, V. B.; Croll, T. I.; et al. Macromolecular structure determination using X-rays, neutrons and electrons: recent developments in \it Phenix. *Acta Crystallogr., Sect. D: Struct. Biol.* **2019**, *75* (10), 861−877.

(28) Arnér, E. S. J.; Zhong, L.; Holmgren, A. Preparation and assay of mammalian thioredoxin and thioredoxin reductase. In *Methods in Enzymology*; Academic Press, 1999; Vol. *300*, pp 226−239.

(29) Daina, A.; Michielin, O.; Zoete, V. SwissADME: a free web tool to evaluate pharmacokinetics, drug-likeness and medicinal chemistry friendliness of small molecules. *Sci. Rep.* **2017**, *7* (1), 42717.

(30) Agnihotri, S.; Mukherji, S.; Mukherji, S. Size-controlled silver nanoparticles synthesized over the range 5−100 nm using the same protocol and their antibacterial efficacy. *RSC Adv.* **2014**, *4* (8), 3974−3983.

(31) Sahu, S. R.; Utkalaja, B. G.; Patel, S. K.; Acahrya, N. Spot Assay and Colony Forming Unit (CFU) Analyses-based sensitivity test for Candida albicans and Saccharomyces cerevisiae. *Bio-Protoc.* **2023**, *13* (21), No. e4872.

(32) Bauer, A. W.; Perry, D. M.; Kirby, W. M. M. Single-disk antibiotic-sensitivity testing of staphylococci; an analysis of technique and results. *AMA Arch. Intern. Med.* **1959**, *104* (2), 208−216.

(33) Jaiswal, S.; Bhattacharya, K.; McHale, P.; Duffy, B. Dual effects of *β*-cyclodextrin-stabilised silver nanoparticles: enhanced biofilm inhibition and reduced cytotoxicity. *J. Mater. Sci.: Mater. Med.* **2015**, *26* (1), 52.

(34) Guo, Y.; Yang, R.; Chen, F.; Yan, T.; Wen, T.; Li, F.; Su, X.; Wang, L.; Du, J.; Liu, J. Triphenyl-sesquineolignan analogues derived from Illicium simonsii Maxim exhibit potent antibacterial activity against methicillin-resistant Staphylococcus aureus (MRSA) by disrupting bacterial membranes. *Bioorg. Chem.* **2021**, *110*, 104824.

(35) O'Boyle, N. M.; Banck, M.; James, C. A.; Morley, C.; Vandermeersch, T.; Hutchison, G. R. Open Babel: An open chemical toolbox. *J. Cheminf.* **2011**, *3* (1), 33.

(36) Morris, G. M.; Huey, R.; Lindstrom, W.; Sanner, M. F.; Belew, R. K.; Goodsell, D. S.; Olson, A. J. AutoDock4 and AutoDockTools4: Automated docking with selective receptor flexibility. *J. Comput. Chem.* **2009**, *30* (16), 2785−2791.

(37) Wang, Z.; Wang, X.; Li, Y.; Lei, T.; Wang, E.; Li, D.; Kang, Y.; Zhu, F.; Hou, T. farPPI: a webserver for accurate prediction of protein-ligand binding structures for small-molecule PPI inhibitors by MM/PB(GB)SA methods. *Bioinformatics* **2019**, *35* (10), 1777−1779.

(38) Wang, Z.; Pan, H.; Sun, H.; Kang, Y.; Liu, H.; Cao, D.; Hou, T. fastDRH: a webserver to predict and analyze protein-ligand complexes based on molecular docking and MM/PB(GB)SA computation. *Briefings Bioinf.* **2022**, *23* (5), bbac201.

(39) Phillips, J. C.; Braun, R.; Wang, W.; Gumbart, J.; Tajkhorshid, E.; Villa, E.; Chipot, C.; Skeel, R. D.; Kalé, L.; Schulten, K. Scalable molecular dynamics with NAMD. *J. Comput. Chem.* **2005**, *26* (16), 1781−1802.

(40) Humphrey, W.; Dalke, A.; Schulten, K. VMD: Visual molecular dynamics. *J. Mol. Graphics* **1996**, *14* (1), 33−38.

(41) Kim, S.; Lee, J.; Jo, S.; Brooks, C. L., III; Lee, H. S.; Im, W. CHARMM-GUI ligand reader and modeler for CHARMM force field generation of small molecules. *J. Comput. Chem.* **2017**, *38* (21), 1879−1886.

(42) Ben Chorin, A.; Masrati, G.; Kessel, A.; Narunsky, A.; Sprinzak, J.; Lahav, S.; Ashkenazy, H.; Ben-Tal, N. ConSurf-DB: An accessible repository for the evolutionary conservation patterns of the majority of PDB proteins. *Protein Sci.* **2020**, *29* (1), 258−267.